Vortex-enhanced propulsion

LYDIA A. RUIZ[1], ROBERT W. WHITTLESEY[2] AND JOHN O. DABIRI[2,3]†

[1]Department of Mechanical Engineering, California Institute of Technology, Pasadena, CA 91125, USA

[2]Graduate Aeronautical Laboratories, California Institute of Technology, Pasadena, CA 91125, USA

[3]Department of Bioengineering, California Institute of Technology, Pasadena, CA 91125, USA

It has been previously suggested that the generation of coherent vortical structures in the near-wake of a self-propelled vehicle can improve its propulsive efficiency by manipulating the local pressure field and entrainment kinematics. This paper investigates these unsteady mechanisms analytically and in experiments. A self-propelled underwater vehicle is designed with the capability to operate using either steady-jet propulsion or a pulsed-jet mode that features the roll-up of large-scale vortex rings in the near-wake. The flow field is characterized by using a combination of planar laser-induced fluorescence, laser Doppler velocimetry and digital particle-image velocimetry. These tools enable measurement of vortex dynamics and entrainment during propulsion. The concept of vortex added-mass is used to deduce the local pressure field at the jet exit as a function of the shape and motion of the forming vortex rings. The propulsive efficiency of the vehicle is computed with the aid of towing experiments to quantify hydrodynamic drag. Finally, the overall vehicle efficiency is determined by monitoring the electrical power consumed by the vehicle in steady and unsteady propulsion modes. This measurement identifies conditions under which the power required to create flow unsteadiness is offset by the improved vehicle efficiency. The experiments demonstrate that substantial increases in propulsive efficiency, over 50 % greater than the performance of the steady-jet mode, can be achieved by using vortex formation to manipulate the near-wake properties. At higher vehicle speeds, the enhanced performance is sufficient to offset the energy cost of generating flow unsteadiness. An analytical model explains this enhanced performance in terms of the vortex added-mass and entrainment. The results suggest a potential mechanism to further enhance the performance of existing engineered propulsion systems. In addition, the analytical methods described here can be extended to examine more complex propulsion systems such as those of swimming and flying animals, for whom vortex formation is inevitable.

Key words: swimming/flying, vortex flows, wakes/jets

---

1. Introduction

Propulsion in air and water at high Reynolds numbers is typically studied by considering the mean (i.e. time-averaged) flow created by the propulsor. In this steady flow approach, the thrust produced by the system is assumed to be dependent only

† Email address for correspondence: jodabiri@caltech.edu

on the mean velocity profiles upstream and in the wake of the propulsor (Prandtl & Tietjens 1934). Variations in the local fluid pressure relative to ambient conditions in the free stream are neglected. The classical expressions for Froude and rocket efficiency, η_f and η_r, respectively, are derived under these conditions (Prandtl 1952; Houghton & Carpenter 2003):

$$\eta_f = \frac{2}{1 + \dfrac{U_w}{U_\infty}}, \tag{1.1}$$

$$\eta_r = \frac{2}{\dfrac{U_w}{U_\infty} + \dfrac{U_\infty}{U_w}} \tag{1.2}$$

where U_∞ and U_w are the free-stream speed and average wake speed relative to the vehicle, respectively. As a consequence of the steady flow assumption, schemes to enhance propulsive efficiency have focused on manipulating the mean velocity profiles upstream and aft of the propulsor. These efforts have included the use of low-RPM propellers (Wu 1962), coaxial contrarotating propellers (Hadler 1969; Cox & Reed 1988), propellers with vane wheels (Grim 1980; Blaurock 1990), ducted propellers (Stipa 1931; Sachs & Burnell 1962), pre- and post-swirl devices (Narita *et al.* 1981; Grothues-Spork 1988) and flow-smoothing devices (Glover 1987). These strategies typically achieve increases in propulsive efficiency of only a few per cent, with a few reports of increases up to 25 % (Breslin & Andersen 1996).

If we remove the assumption of steady flow and allow for spatiotemporal fluctuations of the fluid velocity and pressure, a richer parameter space becomes available to enhance propulsive efficiency. For example, a growing body of literature has suggested that pulsed-jet propulsion and the associated vortex formation can potentially increase propulsive efficiency relative to an equivalent steady jet (Lockwood 1961; Binder & Didelle 1981; Krueger & Gharib 2005; Choutapalli *et al.* 2005; Paxson *et al.* 2006; Krieg & Mohseni 2008; Moslemi & Krueger 2010 and references therein). While the presence of vortex formation is widely recognized in these studies, the mechanisms leading to enhanced performance have only been examined relatively recently. Krueger & Gharib (2003, 2005) have proposed that vortex formation increases the pressure at the exit of the propulsor above the ambient pressure in the free stream. In principle, this has the effect of augmenting the generated thrust or, equivalently, reducing the form drag of the propulsion system.

Additionally, vortex formation has been observed to augment entrainment of ambient fluid in the wake of the propulsor (Hussain & Husain 1989; Dabiri & Gharib 2004; Olcay & Krueger 2008). Since the momentum flux required to overcome drag is proportional to the product of the wake volume and excess wake velocity (i.e. $U_w - U_\infty$; see §2), the recruitment of ambient fluid via entrainment (i.e. increased wake volume) enables the system to support lower wake velocities on average while maintaining a given thrust. The lower wake velocities translate to reduced kinetic energy losses in the wake (for a given thrust), due to the quadratic dependence of wake kinetic energy on wake velocity. Therefore, the ultimate effect of entrainment is to increase propulsive efficiency by reducing the magnitude of kinetic energy losses in the wake (i.e. lower U_w/U_∞ in (1.1) and (1.2)).

In summary, vortex formation can increase propulsive efficiency by increasing the generated thrust via the vortex overpressure in the near-wake and by decreasing the kinetic energy losses in the wake via vortex entrainment.

Previous studies of vortex-enhanced propulsion have not considered the full dynamics of a self-propelled vehicle, focusing instead on the near-wake vortex dynamics of stationary propulsors. The external flow past a moving propulsor is known to affect near-wake vortex formation (Krueger, Dabiri & Gharib 2006) and therefore merits inclusion in order to add relevance to real air and ocean vehicles. Furthermore, previous comparisons between unsteady and steady propulsion have used idealized, theoretical models of steady-jet propulsion when studying unsteady propulsion and vice versa. In this sense, previous comparisons have been indirect. In this paper, we investigate the dynamics of a self-propelled underwater vehicle that is designed to operate in both steady-jet and unsteady vortex formation regimes. The wake is characterized quantitatively in both cases by using planar laser-induced fluorescence (PLIF), laser Doppler velocimetry (LDV) and digital particle-image velocimetry (DPIV). The vehicle performance in steady and unsteady modes is quantified by measuring the Froude propulsive efficiency based on mean wake profiles. The hydrodynamic drag on the vehicle is measured in towing experiments to calculate an alternative propulsive efficiency that considers the work to overcome drag as the 'useful work' in the efficiency definition. In addition, the electrical power consumed by the vehicle is monitored in real-time to estimate the overall vehicle efficiency. This measurement is important because it determines whether the added energy cost of generating flow unsteadiness is compensated by the improved vehicle performance. And yet, it does not appear that this kind of direct measurement in the context of comparisons with steady-jet propulsion has been made previously. We show that, under certain conditions, the energy saved due to increased propulsive efficiency exceeds the energy cost of generating flow unsteadiness. These results can be explained in terms of the wake dynamics, especially the wake vortex overpressure and entrainment.

Section 2 revisits the equations of motion to demonstrate via a control volume analysis the mechanisms whereby vortex formation can augment propulsive efficiency. This derivation extends previous analyses (Krueger 2001) by considering the entire self-propelled vehicle in an arbitrary unidirectional motion and by allowing more general wake kinematics than previously considered. The derivation makes clear the important role of local fluid pressure as a tool for augmenting propulsion in unsteady, incompressible flows. It is further demonstrated that the local fluid pressure in the near-wake can be estimated by employing the concept of vortex added-mass (Krueger & Gharib 2003; Dabiri 2006).

Sections 3 and 4 describe the vehicle design and experimental methods used to study the vehicle, respectively. Measurement results are presented in §5, with special emphasis on the relative performance of the vehicle in unsteady propulsion as compared to the steady propulsion mode. Finally, §6 discusses the results and proposes their extension to other propulsion platforms.

2. Analytical model

To derive a relationship between the propulsive efficiency of a self-propelled vehicle and the characteristics of its near-wake, let us first apply the equations of motion to a control volume surrounding the vehicle. Figure 1 illustrates a submarine vehicle and associated control volume, both inspired by the geometry of the vehicle studied in experiments (see §3).

The control volume has surface normal $\boldsymbol{n}_{sub}$ and is displaced outward from the surface of the vehicle by a distance δ that is comparable to, but greater than, the
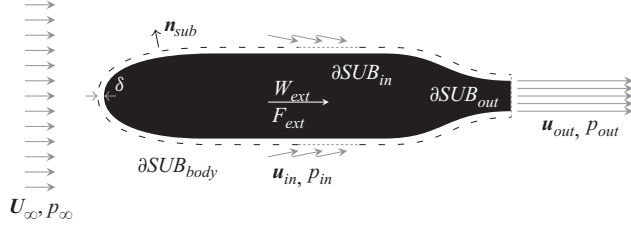
FIGURE 1. Submarine (black silhouette) and associated control volume (dashed and dotted lines). See text for symbol definitions.

boundary-layer thickness. By this construction, the viscous stresses on the vehicle surface are internal to the control volume. However, the effect of skin friction does appear in the difference between the momentum flux entering and exiting the annular region of thickness δ. The force of the propulsor (i.e. propeller) on the fluid is also applied inside the control volume. For the sake of generality, we allow for the possibility of external force $\boldsymbol{F}_{ext}$ and external work W_{ext} applied to the vehicle. In the experiments described in the next section, the dynamic friction between the bearings of the vehicle support strut and the rails of the water tank contributes to $\boldsymbol{F}_{ext}$ and external work, W_{ext}. More generally, $\boldsymbol{F}_{ext}$ is a surrogate for the inertial forces associated with unsteady translation of the vehicle, and it can be considered the force required to constrain the control volume in a steady frame of reference when the vehicle generates a net thrust that would tend to accelerate the vehicle and its control volume. W_{ext} also includes a contribution from the work of the inertial forces.

In the reference frame of the vehicle, the free-stream flow has velocity $\boldsymbol{U}_{\infty}$. Similar to the experimental vehicle, fluid enters the model vehicle at velocity $\boldsymbol{u}_{in}$ and local pressure p_{in} through slots on the lateral surfaces of the vehicle. Fluid exits the vehicle at velocity $\boldsymbol{u}_{out}$ and local pressure p_{out} through a nozzle at the rear. The velocities $\boldsymbol{U}_{\infty}$, $\boldsymbol{u}_{in}$ and $\boldsymbol{u}_{out}$ are generally time-dependent, and $\boldsymbol{u}_{in}$ and $\boldsymbol{u}_{out}$ may be spatially non-uniform across the surfaces ∂SUB_{in} and ∂SUB_{out}, respectively.

The equations expressing conservation of mass, streamwise momentum (henceforth the x-direction) and energy applied to the submarine control volume can be written as

$$\text{mass:} \quad 0 = \rho \oint_{\partial SUB_{out}} \boldsymbol{u}_{out} \cdot \boldsymbol{n}_{sub} \, \mathrm{d}A + \rho \oint_{\partial SUB_{in}} \boldsymbol{u}_{in} \cdot \boldsymbol{n}_{sub} \, \mathrm{d}A, \quad (2.1)$$

$$x\text{-momentum:} \quad F_{ext,x} = \rho \left[\frac{\partial}{\partial t} \int_{SUB} u \, \mathrm{d}V + \oint_{\partial SUB_{out}} u_{out}^2 \, \mathrm{d}A \right] + \oint_{\partial SUB} p \, n_{sub,x} \, \mathrm{d}A, \quad (2.2)$$

$$\text{energy:} \quad \dot{W}_{ext} = \frac{\rho}{2} \frac{\partial}{\partial t} \int_{SUB} |\boldsymbol{u}|^2 \, \mathrm{d}V + \frac{\rho}{2} \oint_{\partial SUB_{in}} |\boldsymbol{u}_{in}|^2 \boldsymbol{u}_{in} \cdot \boldsymbol{n}_{sub} \, \mathrm{d}A$$

$$+ \frac{\rho}{2} \oint_{\partial SUB_{out}} |\boldsymbol{u}_{out}|^2 \boldsymbol{u}_{out} \, \mathrm{d}A + \oint_{\partial SUB_{out}} p \, (\boldsymbol{u}_{out} \cdot \boldsymbol{n}_{sub}) \, \mathrm{d}A, \quad (2.3)$$

where $F_{ext,x}$ and $n_{sub,x}$ are the streamwise scalar components of $\boldsymbol{F}_{ext}$ and $\boldsymbol{n}_{sub}$, respectively; ρ is the fluid density; and the overdot in (2.3) indicates a time derivative. Equations (2.1)–(2.3) assume that the flow is incompressible and adiabatic and that the mass, momentum and energy fluxes through the annular region of thickness δ are negligible relative to the fluxes through the propulsor. In addition, it is assumed that free-stream fluid enters the vehicle through ∂SUB_{in} without appreciable
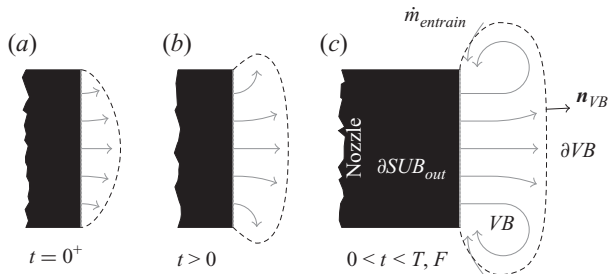
FIGURE 2. (*a–c*) Vortex wake and associated control volume. Nozzle exit is indicated by black silhouette. Dashed line indicates the boundary of forming wake vortex. See text for symbol definitions.

change in speed, such that $|\boldsymbol{u}_{in}| \approx |\boldsymbol{U}_\infty|$ and $p_{in} \approx p_\infty$. Since fluid enters the vehicle nearly perpendicular to the x-direction, the contribution of the inlet flow $\boldsymbol{u}_{in}$ to (2.2) is assumed to be negligible compared with the axial momentum flux across ∂SUB_{out}.

At this stage, classical analyses of steady propulsion employ the assumption that the local pressure around the vehicle, including the pressure in the wake, is approximately equal to the free-stream pressure (Prandtl 1952; Houghton & Carpenter 2003). This assumption eliminates the pressure integrals from (2.2) and (2.3), and leads to the result described in the previous section that the vehicle performance is a function only of the velocity profiles upstream and in the wake. In the present derivation, we will allow for the existence of non-negligible deviations from free-stream pressure at the nozzle exit (i.e. at ∂SUB_{out}); hence, the pressure integrals are retained.

The pressure at ∂SUB_{out} can be related to the wake characteristics by considering a second control volume surrounding the forming wake vortex, as illustrated in figure 2.

During pulsed-jet propulsion, each fluid pulse exiting the vehicle forms a large-scale, coherent vortex. A well-defined boundary exists between the 'vortex bubble' forming at the nozzle exit and the ambient fluid. This has been observed in empirical studies of pulsed jets using dye (Olcay & Krueger 2008) as well as in streamlines (Dabiri & Gharib 2004) and Lagrangian coherent structures (Shadden, Dabiri & Marsden 2006) extracted from PIV data. As illustrated in figure 2, the vortex bubble grows in time until either the end of the fluid pulse at time T or until the vortex ring pinches off from the nozzle at time F, according to the formation number concept of Gharib, Rambod & Shariff (1998). We consider the dynamics of the wake vortex bubble during the interval $0 < t < T, F$.

We treat the vortex boundary ∂VB as a time-dependent material surface that, together with the surface ∂SUB_{out}, bounds a vortex control volume with unit normal $\boldsymbol{n}_{VB}$. Fluid enters the vortex control volume from the exit of the vehicle nozzle and via an entrainment mass flux $\dot{m}_{entrain}$ for which $u_{entrain} \cdot \boldsymbol{n}_{VB} \approx 0$ on ∂VB. This assumption of near-tangential entrainment flow on the surface of the wake vortex, with the entrained fluid ultimately entering the vortex from the rear, is consistent with empirical observations (Maxworthy 1972; Shadden *et al.* 2006; Olcay & Krueger 2008).

Following an analysis similar to that which led to (2.1)–(2.3), and noting that force and work contributions analogous to $\boldsymbol{F}_{ext}$ and W_{ext} (denoted $F_{ext,x}^{VB}$ and W_{ext}^{VB}, respectively) are applied to the control volume VB to maintain the co-moving frame,

FIGURE 3. Combined vehicle–wake control volume. Vehicle is indicated by black silhouette and wake vortex is indicated by grey patch. Dashed and dotted lines indicate the boundary of combined control volume. See text for symbol definitions.

the corresponding equations of motion are

$$\text{mass:} \quad \rho \frac{\partial V_{VB}}{\partial t} + \rho \oint_{\partial SUB_{out}} \boldsymbol{u}_{out} \cdot \boldsymbol{n}_{VB} \, \mathrm{d}A - \dot{m}_{entrain} = 0, \qquad (2.4)$$

$$\text{x-momentum:} \quad \rho \frac{\partial}{\partial t} \int_{VB} u \, \mathrm{d}V + \rho \oint_{\partial SUB_{out}} u_{out}(u_{out} \, n_{VB,x}) \, \mathrm{d}A$$

$$= - \oint_{\partial SUB_{out}} p \, n_{VB,x} \, \mathrm{d}A - \oint_{\partial VB} p \, n_{VB,x} \, \mathrm{d}A + F_{ext,x}^{VB}, \qquad (2.5)$$

$$\text{energy:} \quad \frac{\rho}{2} \left[\frac{\partial}{\partial t} \int_{VB} |\boldsymbol{u}|^2 \, \mathrm{d}V + \oint_{\partial SUB_{out}} |\boldsymbol{u}_{out}|^2 (\boldsymbol{u}_{out} \cdot \boldsymbol{n}_{VB}) \, \mathrm{d}A \right]$$

$$= - \oint_{\partial SUB_{out}} p \, (\boldsymbol{u}_{out} \cdot \boldsymbol{n}_{VB}) \, \mathrm{d}A + \dot{W}_{ext}^{VB}, \qquad (2.6)$$

where V_{VB} in (2.4) is the time-dependent volume of the vortex bubble. Solving each of (2.4)–(2.6) for the flux integral over ∂SUB_{out} and noting that $\boldsymbol{n}_{VB} = -\boldsymbol{n}_{sub}$ on ∂SUB_{out}, we can rewrite (2.1)–(2.3) such that the dependence on flow properties at ∂SUB_{out} is replaced by a dependence on flow properties on ∂VB:

$$\text{mass:} \quad 0 = \rho \frac{\partial V_{VB}}{\partial t} + \rho \oint_{\partial SUB_{in}} \boldsymbol{u}_{in} \cdot \boldsymbol{n}_{sub} \, \mathrm{d}A - \dot{m}_{entrain,} \qquad (2.7)$$

$$\text{x-momentum:} \quad F_{ext,x}^{net} = \rho \frac{\partial}{\partial t} \int_{SUB \cup VB} u \, \mathrm{d}V + \oint_{\partial SUB_{body}} p \, n_{SUB,x} \, \mathrm{d}A + \oint_{\partial VB} p \, n_{VB,x} \, \mathrm{d}A,$$

$$\qquad (2.8)$$

$$\text{energy:} \quad \dot{W}_{ext}^{net} = \frac{\rho}{2} \frac{\partial}{\partial t} \int_{SUB \cup VB} |\boldsymbol{u}|^2 \, \mathrm{d}V + \frac{\rho}{2} \oint_{\partial SUB_{in}} |\boldsymbol{u}_{in}|^2 \boldsymbol{u}_{in} \cdot \boldsymbol{n}_{sub} \, \mathrm{d}A, \qquad (2.9)$$

where $F_{ext,x}^{net}$ and W_{ext}^{net} include the combined inertial force and work contributions, respectively, on the vehicle and vortex wake.

Equations (2.7)–(2.9) correspond to the combined vehicle-wake control volume $SUB \cup VB$ shown in figure 3. We now assume that the flow on the surface $\partial SUB \cup \partial VB$ is irrotational. This condition is satisfied on ∂SUB due to its displacement by δ from the vehicle surface. The assumption of irrotational flow outside ∂VB is similar to the construction of the spherical vortex of Hill (1894) and the Norbury (1973) family of steady vortex rings. It requires that the vorticity remain compact and that the time scale of vorticity diffusion remain large relative to the time scale of vortex formation. The latter condition is satisfied for high-frequency Reynolds numbers of the pulsed jet, i.e. $Re_\omega = \omega L_p^2 / \nu \gg 1$, where ω is the frequency of pulsation, L_p is the length of

the slug of fluid ejected during each pulse, and ν is the kinematic viscosity of the fluid.

When the assumption of irrotational flow on the surface $\partial SUB \cup \partial VB$ is satisfied, the pressure integrals in (2.8) can be rewritten in terms of the velocity potential ϕ and the local flow speed $|\boldsymbol{u}|$ by using the unsteady Bernoulli equation (Saffman 1992):

$$p = \rho \left[C(t) - \frac{\partial \phi}{\partial t} - \frac{1}{2}|\boldsymbol{u}|^2 \right], \qquad (2.10)$$

where C is the time-dependent Bernoulli constant. We assume that $\partial SUB \cup \partial VB$ forms a single streamsurface and with a single associated value of the Bernoulli constant. This assumption is violated at the inlets to the submarine, where flow crosses from the free stream into the vehicle. However, in practice the inlets represent only 1 % of the vehicle surface area, and they are confined to narrow streamwise strips at discrete azimuthal positions (see §3); hence, the breakdown of the streamsurface assumption is highly localized. Substituting (2.10) into (2.8) gives

$$\text{mass:} \quad 0 = \rho \frac{\partial V_{VB}}{\partial t} + \rho \oint_{\partial SUB_{in}} \boldsymbol{u}_{in} \cdot \boldsymbol{n}_{sub} \, \mathrm{d}A - \dot{m}_{entrain,} \qquad (2.11)$$

$$\text{x-momentum:} \quad F_{ext,x}^{net} = \rho \frac{\partial}{\partial t} \int_{SUB \cup VB} u \, \mathrm{d}V - \rho \oint_{\partial SUB_{body}} \frac{\partial \phi}{\partial t} n_{SUB,x} \, \mathrm{d}A$$

$$- \frac{\rho}{2} \oint_{\partial SUB_{body}} |\boldsymbol{u}|^2 n_{SUB,x} \, \mathrm{d}A - \rho \oint_{\partial VB} \frac{\partial \phi}{\partial t} n_{VB,x} \, \mathrm{d}A$$

$$- \frac{\rho}{2} \oint_{\partial VB} |\boldsymbol{u}|^2 n_{VB,x} \, \mathrm{d}A, \qquad (2.12)$$

$$\text{energy:} \quad \dot{W}_{ext}^{net} = \frac{\rho}{2} \frac{\partial}{\partial t} \int_{SUB \cup VB} |\boldsymbol{u}|^2 \, \mathrm{d}V + \frac{\rho}{2} \oint_{\partial SUB_{in}} |\boldsymbol{u}_{in}|^2 \boldsymbol{u}_{in} \cdot \boldsymbol{n}_{sub} \, \mathrm{d}A. \qquad (2.13)$$

While the wake vortex remains attached to the vehicle (i.e. $0 < t < T, F$), we may approximate the flow speed on $\partial SUB \cup \partial VB$ as $|\boldsymbol{u}| \approx U_\infty$. This constant speed can be taken outside the flux integrals in (2.12), which allows them to be rewritten as

$$- \left(\frac{\rho}{2} U_\infty^2 \oint_{\partial SUB_{body}} n_{SUB,x} \, \mathrm{d}A + \frac{\rho}{2} U_\infty^2 \oint_{\partial VB} n_{VB,x} \, \mathrm{d}A \right) = 0 \qquad (2.14)$$

since the integral of $\boldsymbol{n} \, \mathrm{d}A$ is zero by definition on a closed surface. The time derivatives of the velocity potential in (2.12) can be taken outside of their respective derivatives. We can then make use of the added-mass definition for streamwise motion:

$$- \oint_{\partial V} \phi n_x \, \mathrm{d}A = \alpha_{xx} V U_x, \qquad (2.15)$$

where V is the volume enclosed by the surface ∂V, U_x is the speed of the volume centroid in the streamwise direction and α_{xx} is the added-mass coefficient for streamwise motion (Saffman 1992). Note that for more general motions, including combinations of translation and rotation, the full added-mass tensor must be considered (Batchelor 2000). Applying (2.14) and (2.15) to (2.12) and evaluating

the time derivatives, we arrive at the following set of equations:

$$\text{mass:} \quad 0 = \rho \dot{V}_{VB} + \rho \oint_{\partial SUB_{in}} \boldsymbol{u}_{in} \cdot \boldsymbol{n}_{sub} \, \mathrm{d}A - \dot{m}_{entrain}, \tag{2.16}$$

$$x\text{-momentum:} \quad F_{ext,x}^{net} = \rho \left(1 + \alpha_{xx}^{SUB}\right) \dot{U}_x^{SUB} V_{SUB} + \rho \frac{\partial}{\partial t} \left[\left(1 + \alpha_{xx}^{VB}\right) U_x^{VB} V_{VB} \right], \tag{2.17}$$

$$\text{energy:} \quad \dot{W}_{ext}^{net} = \rho \left[U^{SUB} \dot{U}^{SUB} V_{SUB} + U^{VB} \dot{U}^{VB} V_{VB} + \frac{1}{2} \left(U^{VB}\right)^2 \dot{V}_{VB} \right], \tag{2.18}$$

where superscripts are used to indicate properties of the vehicle (i.e. SUB) or wake (i.e. VB). Equation (2.18) assumes that the growth rate of the wake vortex is primarily determined by ambient fluid entrainment, i.e. $\rho \dot{V}_{VB} \approx \dot{m}_{entrain}$. This is the case for vortex rings formed with small values of vortex formation time T and for flows with rapid jet initiation and termination (Dabiri & Gharib 2004; Olcay & Krueger 2008). In these cases, the second term in (2.13), which can be rewritten by multiplying (2.11) by U_∞^2, is approximately zero. Since $\boldsymbol{u}_{in} \cdot \boldsymbol{n}_{sub} < 0$ at the inlets, (2.18) is an overestimate of $\dot{W}_{ext}^{net}$ if wake vortex growth is not dominated by ambient fluid entrainment.

The form of (2.17) is particularly useful for understanding how near-wake vortex formation affects propulsion. In the absence of external forces (i.e. $F_{ext,x} = 0$), the forward acceleration of the vehicle (and its added-mass, which is proportional to α_{xx}^{SUB}) is wholly dependent on the rearward acceleration of the vortex bubble. Since the evolution of the vortex bubble is temporally asymmetric relative to the peak vortex bubble size (cf. figure 2), with maximum flow accelerations occurring during initial vortex formation, the enhancement of propulsion by vortex formation persists even when considering time-averaged wake dynamics. In the standard equations of motion (2.1)–(2.3), this is reflected in a non-zero contribution from the pressure integral over ∂SUB_{out} (Krueger 2001) as well as a wider wake velocity profile.

Entrainment of ambient fluid can be viewed as contributing to propulsion by enhancing the size and growth rate of the vortex bubble (cf. (2.16)). The vortex added-mass makes an explicit contribution to propulsion via the added-mass coefficient α_{xx}^{VB} in (2.17). To be sure, the wake kinetic energy is also increased due to vortex formation, since the wake is larger than it would be in the case of an equivalent steady jet. However, as we will see in the following sections, this added energy cost to generate flow unsteadiness can be fully compensated by the increased vehicle thrust under certain conditions. These trade-offs are captured by the propulsive efficiency, which can be defined in general as

$$\eta = \frac{\langle F_{ext,x}^{net} U^{SUB} \rangle}{\langle \dot{W}_{ext}^{net} \rangle}, \tag{2.19}$$

where $\dot{W}_{ext}^{net}$ is presently taken as the shaft power delivered to the vehicle and the angle brackets denote time averages over the duration T of vortex formation. Substituting (2.17) and (2.18) into (2.19) gives

$$\eta = \frac{\left\langle \left\{ \left(1 + \alpha_{xx}^{SUB}\right) \dot{U}_x^{SUB} V_{SUB} + \frac{\partial}{\partial t} [(1 + \alpha_{xx}^{VB}) U_x^{VB} V_{VB}] \right\} U^{SUB} \right\rangle}{\left\langle \left[U^{SUB} \dot{U}^{SUB} V_{SUB} + U^{VB} \dot{U}^{VB} V_{VB} + \frac{1}{2} (U^{VB})^2 \dot{V}_{VB} \right] \right\rangle}. \tag{2.20}$$

Equation (2.20) represents the most general expression for the efficiency of unsteady propulsion, subject to the aforementioned assumptions used in its derivation. When vortex formation occurs at a sufficiently high frequency, the mass of the vehicle acts
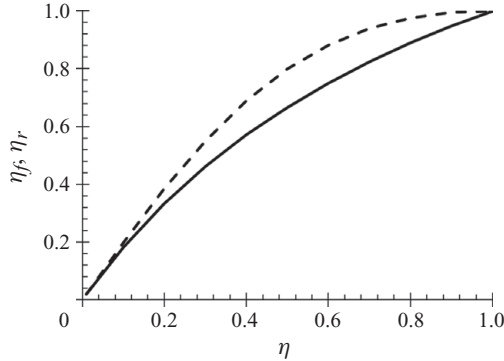
FIGURE 4. Froude (η_f, solid curve) and rocket (η_r, dashed curve) efficiencies as a function of the unsteady efficiency (η) for $\alpha_{xx}^{VB} = 1/2$.

as a low-pass filter on its dynamics, resulting in a quasi-steady forward motion. In this case, $\dot{U}^{SUB} \approx 0$ and (2.20) can be further reduced to

$$\eta \approx \frac{\left\langle \frac{\partial}{\partial t}\left[\left(1 + \alpha_{xx}^{VB}\right)U^{VB}V_{VB}\right]U^{SUB}\right\rangle}{\left\langle U^{VB}\dot{U}^{VB}V_{VB} + \frac{1}{2}(U^{VB})^2\dot{V}_{VB}\right\rangle}. \tag{2.21}$$

In the limit of quasi-steady flow, the time derivative of a given quantity ξ in (2.21) can be approximated as $\partial\xi/\partial t = f_p\xi(T)$, where f_p is the frequency of jet pulsing and $\xi(T)$ is the value of the property ξ when vortex formation is complete. Also, the vehicle and wake vortex velocities can be approximated as U_∞ and U_w, respectively. These simplifications result in an expression that is only dependent on the added-mass coefficient and the velocity ratio U_w/U_∞:

$$\eta \approx \frac{2}{3}\left(1 + \alpha_{xx}^{VB}\right)\frac{U_\infty}{U_w}. \tag{2.22}$$

Figure 4 plots the relationship between this quasi-steady version of the efficiency metric derived presently and the Froude and rocket efficiencies given in (1.1) and (1.2), respectively. We note that all three of the efficiency definitions coincide at $\eta = 0$ and $\eta = 1$ for $\alpha_{xx}^{VB} = 1/2$, which corresponds to spherical wake vortex formation. In general, however, the upper limits of the three definitions do not coincide, reflecting the different assumptions made in deriving each one.

The analytical model developed here motivates our subsequent focus on empirical measurements of vortex entrainment and added-mass dynamics in the near-wake of a self-propelled vehicle. To enable direct comparisons with steady propulsion, we will make use of the standard efficiency definitions (e.g. (1.1)), while using the new relations derived from this analytical model to identify the relative contributions of vortex entrainment and added-mass to unsteady propulsion.

3. Vehicle design

3.1. *Vehicle configuration and components*

A schematic diagram of the underwater vehicle studied in experiments is shown in figure 5. The vehicle is 102.3 cm long with a maximum diameter of 15.2 cm. Its
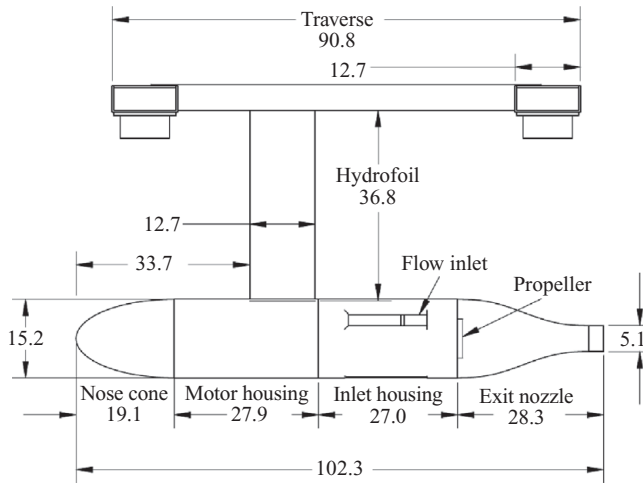
FIGURE 5. Schematic diagram of vehicle components including horizontal traverse. Dimensions are in cm.

profile was inspired by a conventional submarine design, but no attempt was made to optimize the hydrodynamic characteristics of the vehicle. Instead, priority was given to designing a vehicle that enables both steady- and pulsed-jet propulsion with minimal changes to the configuration, so that the relative performance of the vehicle in both modes can be directly compared. The design features that accomplish steady and unsteady propulsion are described in detail in § 3.2.

The primary components of the vehicle are an anterior, water-flooded nose cone, waterproof motor housing with attached hydrofoil support strut, water-flooded inlet housing and a posterior exit nozzle connected to the inlet housing. Each of these components was constructed from glass-reinforced plastic with a wall thickness of 0.3 cm. The nose cone serves as a static ballast to reduce the natural positive buoyancy of the vehicle. Remaining vertical loads due to deviation from the trim condition are taken by the bearings that connect the vehicle to the water tank (see below).

The waterproof motor housing contains a 2 hp DC motor (AstroFlight Cobalt 60) that drives the vehicle propeller and, where applicable, the pulsed-jet mechanism described in the next section. The voltage range for the motor is 24–36 V with maximum continuous current of 35 A. Electrical power is supplied to the motor from an external power supply (Agilent 6674A) via a flexible cable that passes through the hydrofoil support strut. The cable is significantly longer than the distance of vehicle travel in the water tank (≈ 20 m), so that it does not interfere with the self-propulsion of the vehicle. A previous design iteration utilized onboard power from a sealed lead acid battery; however, it was found that the voltage across the motor decayed too rapidly to effectively characterize the vehicle performance in repeated experiments. A companion cable transmits motor speed data via an optical tachometer (Monarch Instruments) in the motor housing that continuously scans the motor shaft. As a practical matter, a third cable is connected to a moisture sensor (Watchdog) in the motor housing in order to detect leaks.

The motor throttle is regulated by a speed controller (AstroFlight) connected to the motor. Communication with the speed controller is achieved through a radio-frequency receiver (Polk's Hobby Seeker 6). The current drawn by the motor is measured via a current clamp (Fluke), which outputs 1 mV per input ampere of

current. The measurement accuracy of the device is $\pm 2\,\%$ of the reading $\pm 0.5\,\mathrm{A}$. During self-propulsion, the motor typically draws 12 A at 37 V. A large fraction of this power is dissipated within the long power transmission cables that connect the vehicle to external power. However, as mentioned above, the emphasis of this study is on the relative performance of the steady and unsteady propulsion modes. Since the system inefficiencies are equally applied to both modes of propulsion (cf. § 3.2), they are deemed acceptable in this study.

A symmetric vertical hydrofoil with approximately 13 % thickness (relative to chord length) is connected to the motor housing by epoxy, forming a waterproof seal. In addition to providing a conduit for power and data from the motor housing, the hydrofoil provides the structural connection between the vehicle and a traverse that rolls along the horizontal rails of the water tank. Hence, the vehicle is constrained to unidirectional motion parallel to the rails of the water tank. Visual inspection confirmed that no significant free-surface waves were generated by the hydrofoil or the proximal portions of the vehicle hull.

The flow inlets to the vehicle are located on a housing attached directly downstream from the motor housing. Flow enters the inlet housing through one to three rectangular slots equally spaced around the azimuth of the housing. Each slot is $15.2 \times 2.5\,\mathrm{cm}$ and aligned with the flow direction. The cross-stream edges of the slots are rounded to promote smooth inlet flow. Fluid is drawn into the inlet housing by a fixed pitch, 7.6 cm diameter, 7-blade, brass skew propeller that is connected to the motor at a 1:1 gear ratio. The propeller is located downstream from the inlet slots at the junction between the inlet housing and the exit nozzle. The specific propeller used in this study is not optimized for operation in the shrouded configuration. It was selected solely due to its ability to generate sufficient thrust for self-propulsion in the range of vehicle speeds studied here. As with the power transmission described above, any propeller inefficiency was deemed acceptable since it was consistent for the steady and unsteady propulsion modes and therefore did not affect the relative comparisons between modes.

The exit nozzle diameter (D_{out}) contracts from 15.2 cm to 5.1 cm over its 28.3 cm length. Its shape is derived from a sixth-order polynomial curve fit. Flow visualization using tufts and dye confirmed that the flow external to the nozzle remains attached.

The vertical hydrofoil of the vehicle is mounted onto a horizontal traverse, constructed as an I-beam configuration from anodized aluminium tubing with $5.1 \times 12.7\,\mathrm{cm}$ rectangular cross-section and 0.3 cm wall thickness. The traverse rests on four low-friction roller bearing pillow blocks (Lee Linear), which have an average rolling friction coefficient of 0.004.

3.2. *Mechanisms of steady and unsteady propulsion*

To modulate the steadiness of the jet efflux, a mechanism was designed to periodically occlude portions of the slots on the inlet housing. A planetary gear assembly connects the motor shaft to a hollow cylindrical shell that rotates inside the inlet housing. The outer surface of the rotating shell is flush with the inner surface of the inlet housing. The planetary gear assembly reduces the speed of shell rotation by a factor of 5 relative to the motor speed.

The rotating shell itself has a set of open slots around the azimuth; the slot width determines the solidity of a given shell design. As the shell rotates, the solid portion of the shell periodically blocks the inlet slots, preventing inlet flow and consequently throttling the exit flow (figure 6). A $2.5 \times 1.7\,\mathrm{cm}$ portion of each inlet slot is left unblocked at all times to avoid cavitation due to the pressure drop that occurs during
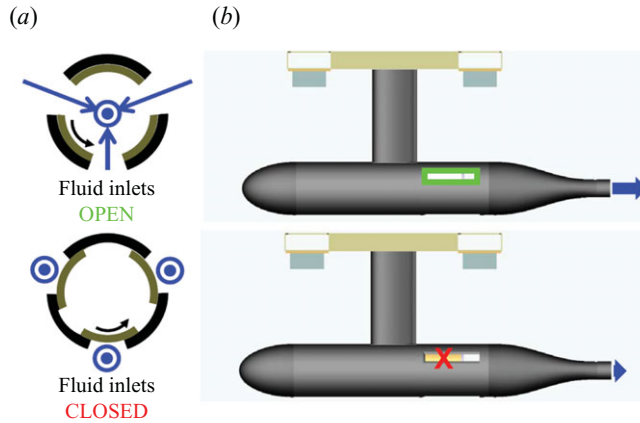
(*a*)   (*b*)

FIGURE 6. Principle of operation for unsteady, pulsed-jet configuration. (*a*) View from aft of inlet housing. Outer black arcs indicate inlet housing and inner brown arcs indicate rotating cylindrical shell. Black arrows indicate direction of inner shell rotation. Blue arrows indicate flow direction (bullseyes are vectors out of the page). (*b*) Side views of the vehicle corresponding to stages in (*a*). Green box indicates open inlet, red X indicates blocked inlet and blue arrows at the jet exit indicate magnitude of jet efflux.

(*a*)   (*b*)
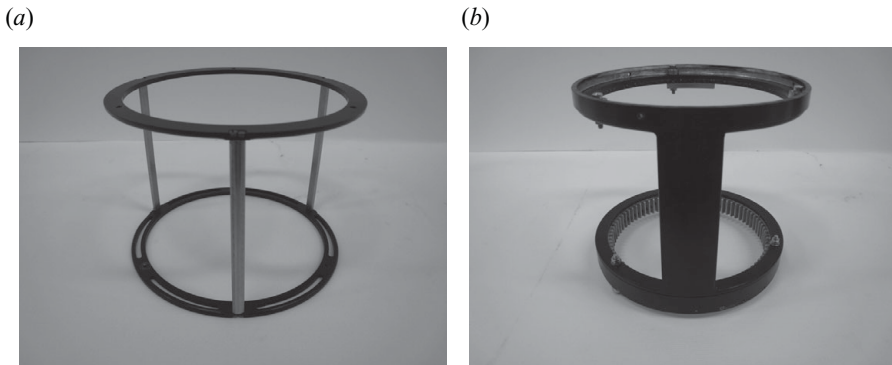
FIGURE 7. Images of cylindrical rotating shells for steady-jet (*a*) and pulsed-jet (*b*) vehicle configurations. Shell diameter is 15.2 cm in each case.

slot blockage. Visual inspection confirmed that this strategy prevented the occurrence of flow cavitation in the inlet housing.

The solidity of the rotating shell (i.e. the fraction of the shell surface area composed of solid material) and its rotational speed determine the level of inlet flow blockage and, by fluid continuity, the level of pulsation of the exit flow. The advantage of manipulating the flow upstream of the propeller is that the vortical structures generated in the near-wake do not directly interact with the physical mechanism that generates unsteady flow. This is in contrast to alternative flow-chopping or nozzle-blocking schemes that could also be implemented at the nozzle exit, but that can potentially create unwanted secondary vorticity.

To generate nominally steady flow, a shell design with minimal solidity ($<2\%$) was used. This shell consisted of two thin rings at the bases of the cylindrical shell, connected by three 27 cm $\times$ 0.6 cm support spars spaced equally around the azimuth (figure 7*a*). Mass was added to the bases of each shell to ensure that the total moment

of inertia was evenly distributed around the azimuth with a value of $4.6\,kg\,cm^2$ in each case. Therefore, the power required to rotate the shell in the steady and unsteady propulsion modes is kept constant.

In most of the experiments described in this paper, the vehicle was operated using a single inlet slot at the bottom of the inlet housing. The frequencies of jet pulsation corresponding to this slot design varied with motor rotation rate ($\times 1/5$) from 0 to 13 Hz. Figure 7(*b*) shows the shell design most commonly used for unsteady propulsion experiments. The solid portion of the shell subtends $26°$ around the circumference. This design corresponds to dimensionless vortex ring formation times $\hat{T} = U_w T / D_{out}$ between 2.5 and 3.4, with lower values of $\hat{T}$ occurring at higher motor speeds. This range of vortex formation times leads to the formation of a single, coherent vortex ring during each flow pulse (Gharib *et al*. 1998).

4. Experimental methods

4.1. *Test facility*

Experiments were conducted in a 40 m long free-surface water tank at the California Institute of Technology. The tank cross-section is 1.1 m wide and 0.6 m deep. The vehicle was positioned in the centre of the tank cross-section and its horizontal traverse was connected to two 3.8 cm diameter rails above the tank on opposite sides. The rails run the full length of the water tank; therefore, the vehicle was capable of travelling the full length of the tank in principle. Typically, 5–20 m of vehicle travel was measured in performance tests. The relatively long length of the tank allowed the vehicle to achieve a steady-state velocity before each set of measurements was initiated. A motorized traverse was programmed using proportional-integral control (LabVIEW 8.5) to follow the vehicle traverse at a specified distance (typically $\approx 0.5\,m$) determined by an infrared distance sensor (Sharp). This traverse was used to carry auxiliary equipment for power monitoring and flow visualization. Power and data transmission to the vehicle and auxiliary traverse were accomplished from a stationary console located at the midpoint of the water tank.

4.2. *Planar laser-induced fluorescence measurements*

Planar laser-induced fluorescence (PLIF) was used for qualitative visualization of the near-wake flow in the steady- and pulsed-jet modes. The principal objective of these measurements and the DPIV measurements described in §4.3 was to verify that the pulsed-jet mode does indeed create large-scale coherent vortex rings in the near-wake. The near-wake of the vehicle was also studied in the steady-jet mode to verify that the jet resembled a conventional round turbulent jet without any coherent large-scale vortex formation that could be attributed to flow pulsation at the shell rotation frequency or its harmonics. For these measurements, the vehicle was held stationary by collar clamps placed fore and aft of each of the pillow blocks connecting the traverse to the water tank rails (figure 8).

Rhodamine 6G, a fluorescent dye with maximum absorption near 530 nm and emission near 555 nm, was manually injected into a slot of the inlet housing (i.e. the portion that remains continuously unblocked, cf. §3.2) using a syringe connected to Tygon tubing. Dye was continuously injected with negligible momentum flux for the duration of each test. The dye was excited at 532 nm by two Nd:YAG lasers (New Wave) with a power rating of $30\,mJ\,pulse^{-1}$. The output laser beam was collimated into a 2 mm thin sheet by a cylindrical lens and then re-directed $90°$ by a mirror to illuminate the symmetry plane of the near-wake. This laser path involved
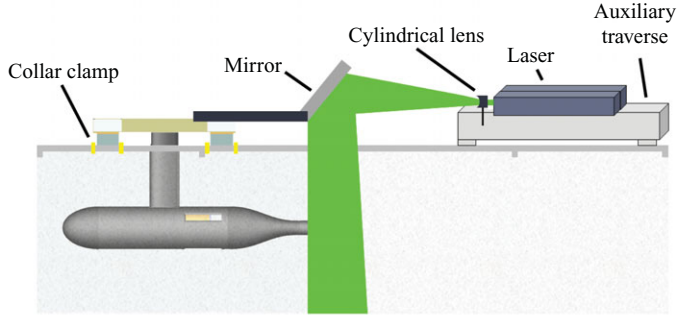
FIGURE 8. Schematic diagram of the set-up for near-wake flow visualization of the stationary vehicle. Laser sheet is illustrated in green.

the transmission of the laser beam through the free surface of the water. Since the vehicle was held stationary, flow disturbances at the free surface were negligible. Positively buoyant particles at the free surface did occasionally reflect incident laser light, causing streakiness of the laser sheet in the field of view. However, this artefact did not affect interpretation of the PLIF images or processing of DPIV data. The laser and associated optics were held on the auxiliary traverse located on the water tank rails downstream from the vehicle.

A 60 mm lens was used in conjunction with a 1024×1024 CMOS video camera (Photron APX-RS) for flow imaging. A band-pass filter (Lee Filter) allowing transmission between 550 and 700 nm was placed over the camera lens to block extraneous Mie scattering from particulates in the water. The field of view was 3 jet diameters in the axial direction and 1.3 jet diameters in the radial direction in each test.

Image capture was triggered by a 5 V TTL signal from the laser upon each firing of the Q-switch. Firing of the Q-switch and subsequent image acquisition could not be synchronized with the phase of rotation of the cylindrical shell due to technical limitations of the experiment. In tests of unsteady propulsion, the phase could be inferred *a posteriori* based on the size of the forming vortex ring in the near-wake. This could not be accomplished in the case of steady propulsion, since the near-wake did not exhibit a well-defined periodicity related to the shell rotation. For the purpose of the PLIF measurements, namely the qualitative validation of near-wake structure, the lack of *a priori* phase information was inconsequential.

4.3. *DPIV measurements*

A more quantitative evaluation of the near-wake of the steady- and pulsed-jet modes was provided by DPIV measurements. For these measurements, the vehicle was again held in a stationary position, and the laser beam path was as illustrated in figure 8. Krueger *et al.* (2006) have previously conducted DPIV studies of vortex ring formation in a co-flow, a process analogous to measurements on a forward-translating vehicle. They observed that the external flow reduces the maximum size of forming vortex rings, although the effect is modest for $U_\infty/U_w < 0.5$. Both the steady- and pulsed-jet flows studied in this paper remain in the range $U_\infty/U_w < 0.5$. Therefore, we do not expect the qualitative flow structure to change between stationary and self-propelled tests. The quantitative differences that occur due to forward translation of the vehicle will be evaluated using LDV measurements of the moving vehicle (§ 4.4).

The water tank was seeded with neutrally buoyant, silver-coated, hollow glass spheres with a nominal diameter of 13 µm (Potters Industries). For DPIV measurements, the two lasers were fired with a relative time delay of 5.3–21.2 ms, with smaller time delays at higher jet speeds to limit the displacement of particles between successive images. A 60 mm lens was typically used in steady-jet tests, while both 60 and 105 mm lenses were used for pulsed-jet tests in order to increase the spatial resolution of the measured near-wake vortex rings.

To limit out-of-plane flow due to swirl created by the propeller, a honeycomb screen was placed in the exit of the jet nozzle. The flow straightener was 2.0 in. in length and 2.0 in. in diameter, with a 0.125 in. diameter cell size. Inspection of the raw DPIV vector plots confirmed that the flow straightener effectively reduced the out-of-plane flow and associated particle image loss. During self-propulsion experiments, the honeycomb was removed to avoid the associated pressure loss from flow blockage and to increase the overall vehicle performance. The removal of the honeycomb led to additional swirl in the wake due to propeller rotation. Previous research on post-swirl devices predicts a reduction of 1–9 % in propulsive efficiency due to the presence of this swirl (Breslin & Andersen 1996). However, this loss was smaller than that associated with the honeycomb.

Particle images were processed using an in-house DPIV code. Steady-jet measurements were post-processed using a 32×32 pixel interrogation window and a 16×16 pixel step size. Pulsed-jet measurements collected using a 105 mm lens were post-processed using a 64×64 pixel interrogation window and a 32×32 pixel step size. The field of view encompassed by these unsteady flow measurements included only the top half of the near-wake at higher spatial resolution. Once it was evident that the pulsed-jet configuration produced vortex ring roll-up in the near-wake as designed, the 60 mm lens and associated DPIV processing parameters were used to verify the axial symmetry of the vortex rings by measuring the full wake width.

4.4. *LDV measurements*

LDV was used to measure the mean velocity profiles in the near-wake during steady and unsteady self-propulsion. Since LDV is a pointwise technique, the spatial velocity profiles were constructed from repeated tests of the vehicle, with a subset of the full profile collected during each run.

A one-component velocimeter (Measurement Science Enterprise miniLDV) was used in the experiments. The system resolves flow speeds from 1 mm s^{-1} to 300 m s^{-1} with a measurement uncertainty of ± 0.1 %. The raw signal-to-noise ratio (S:N) of the measurements was monitored in real-time, and only data with S:N > 4 were accepted. An aluminium probe strut was designed to mount the LDV at the rear of the vehicle traverse, as shown in figure 9. The probe strut was attached to a 100 mm vertical translation stage, thus allowing the LDV probe volume to translate in the vertical direction across the nozzle exit. The vertical stage was mounted to a horizontal 100 mm stage through a 90° bracket plate. This second translation stage allowed for movement of the probe volume in the horizontal direction. The scanning paths of both translation stages were controlled by commercial software (Measurement Science Enterprise). For the majority of measurements described in this paper, the LDV probe volume was located 0.25 jet diameters downstream from the nozzle exit plane. Measurements at this axial location were found to be representative of the near-wake velocity profiles.

LDV measurement data were transferred in real-time to a PC located on the auxiliary traverse, which automatically followed behind the vehicle at a fixed distance
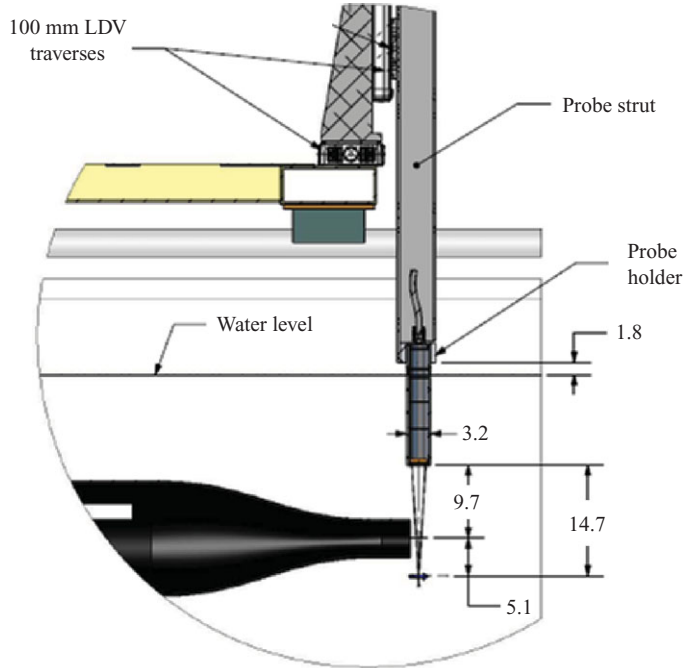
FIGURE 9. (Colour online) Schematic diagram of the LDV assembly mounted onto the vehicle traverse. Vertical LDV traverse is shown in the extreme low position. Dimensions are in cm.

(cf. §4.1). Post-processing to construct full spatial velocity profiles from the samples collected during each vehicle run was accomplished manually.

4.5. *Hydrodynamic drag measurements*

Measurements of the hydrodynamic drag on the underwater vehicle were conducted to support subsequent calculations of propulsive efficiency (§4.6). Force measurements were obtained using a load cell (Omega) with 22.2 N maximum capacity. The load cell was used in compression, for which the measurement accuracy is $\pm 0.15\,\%$ of the full scale.

The maximum output of the load cell without amplification is 10 mV. This signal was amplified using a signal conditioner (Omega Bridgesensor) with a frequency response of 2 kHz and gain between 40 and 250. The load cell was calibrated under compression by applying loads across the full range of sensor capacity; the linearity of the output signal with input load was verified.

The load cell was mounted between the auxiliary motorized traverse and the vehicle traverse using a swivel-bearing design to eliminate off-axis loads. The auxiliary traverse was programmed to travel forward at a series of constant speeds between 10 and $60\,\mathrm{cm\,s^{-1}}$, pushing the vehicle traverse ahead of it. Measurements were conducted with and without the vehicle attached to its traverse in order to distinguish between hydrodynamic drag and resistance due to traverse friction. The measured traverse friction was subtracted from the total resistance at the load cell to determine the hydrodynamic drag on the vehicle. The resulting measurements of drag coefficient versus Reynolds number are plotted in figure 10.

Since the hydrodynamic drag and traverse friction were comparable in magnitude, the uncertainty of the hydrodynamic drag computed by the subtraction technique described above was of the same order of magnitude as the drag itself. The
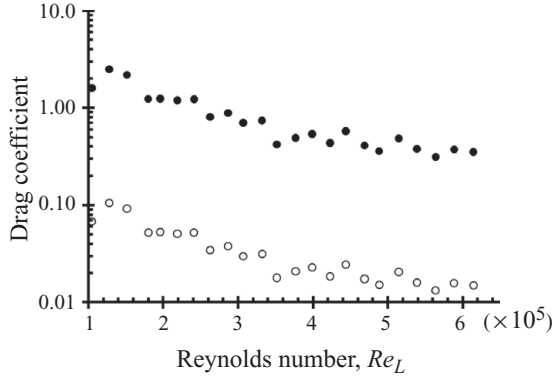
FIGURE 10. Vehicle hydrodynamic drag versus Reynolds number. Drag coefficients are computed based on frontal area (solid circles) and wetted surface area (open circles). Reynolds number is calculated using the vehicle length. Measurement uncertainty is of the same order of magnitude as the data points due to the subtraction technique used to compute the vehicle drag (see text).

trend in drag coefficient with increasing Reynolds number should therefore be viewed cautiously, especially in the light of its difference from the trends found in measurements of canonical shapes (Schlichting & Gersten 2000). Nonetheless, the magnitude of the measured drag coefficients is consistent with published data for similarly shaped bodies in this range of Reynolds numbers (Hoerner 1965). Furthermore, we will show in §5.2 that the conclusions garnered from the propulsive efficiency calculation based on hydrodynamic drag are supported by Froude efficiency measurements based on (1.1) and the unsteady efficiency model in (2.21).

4.6. *Vehicle performance test protocols and metrics*

Propulsive performance tests were conducted for three vehicle configurations: (i) steady propulsion in the absence of a cylindrical rotating shell in the inlet housing, (ii) steady propulsion using the low-solidity rotating shell in the inlet housing (i.e. figure 7a) and (iii) unsteady propulsion using the cylindrical shell shown in figure 7(b). At least 15 tests of the vehicle in each configuration were conducted in order to construct the full spatial velocity profiles across the nozzle exit of the moving vehicle using LDV. The maximum vehicle speed in these tests was 0.4 m s^{-1}. To access higher vehicle speeds, approaching 0.6 m s^{-1}, a second set of experiments was conducted using a new version of the same motor (AstroFlight Cobalt 60) at higher shaft speeds. The higher speed tests were conducted using only configurations (i) and (iii) described above. Twelve tests of the vehicle in each of these configurations were conducted.

Ambient fluid entrainment in the near-wake was quantified by an entrainment ratio defined as

$$\zeta = \frac{Q}{Q_{out}} = \frac{\int_0^{2\pi} \int_0^{R_{out}} u_{out,x}(r) r \, dr \, d\theta}{U_w A_{out}}, \qquad (4.1)$$

where R_{out} is the radius of the nozzle exit and θ is the azimuth angle. An entrainment ratio of 1 corresponds to a top-hat jet efflux with no ambient fluid entrainment.

The propulsive efficiency of the vehicle was measured using both (1.1) and a drag-based hydrodynamic efficiency:

$$\eta_h = \frac{F_D U^{SUB}}{F_D U^{SUB} + (1/2)\rho A_{out} U_w (U_w - U_\infty)^2},$$

(4.2)

where F_D is the drag on the vehicle. This expression for propulsive efficiency considers the 'useful work' to be that required to overcome hydrodynamic drag. The inefficiency of propulsion is assigned to the excess kinetic energy in the wake, which is proportional to $(U_w - U_\infty)^2$.

Finally, the total electrical power consumed by the vehicle in each test was quantified by a power consumption coefficient:

$$C_p = \frac{IV}{\frac{1}{2}\rho A_{out} U_\infty^3},$$

(4.3)

where I is the current drawn by the motor and V is the voltage across the motor.

4.7. Motor calibrations

Most of the results presented in §5 are given as a function of motor speed. This choice of independent variable allows for the most direct comparison between the steady and unsteady propulsion modes, since the motor is the consistent input in each case. In addition, the motor speed provides an implicit characterization of the unsteady jet pulsing frequency. Since the cylindrical rotating shell is geared down from the motor at a fixed 1:5 ratio, the jet pulsing frequency (in Hz) can be deduced from the motor speed (in r.p.m.) by dividing the latter by $60 \times 5 = 300$. Finally, we note that the motor speed is measured with much smaller uncertainty ($<1\%$) than alternative choices of independent variable such as the vehicle or wake speed.

However, to enable interpretation of the results in terms of these alternative independent variables, figure 11 plots the vehicle speed, wake speed and vortex formation time versus motor speed for the self-propelled vehicle tests. The wake speed and vortex formation time were calculated based on the centreline velocity at a distance 0.25 jet diameters from the nozzle exit plane. The jet efflux exhibited a nearly top-hat velocity profile across the nozzle exit at this distance, making the centreline velocity representative of the average wake velocity. The measurement uncertainty in the vehicle velocity was approximately 15%, and the turbulence fluctuations in the average wake speed varied from 16% in the low-speed (i.e. motor 1), steady-jet tests to 30% in the high-speed (i.e. motor 2), unsteady-jet tests.

5. Results

5.1. Stationary vehicle near-wake

Figure 12 shows representative images of the near-wake of the stationary vehicle with steady (figure 12a) and unsteady (figure 12b) cylindrical shell designs rotating inside the inlet housing. The near-wake of the steady flow is characterized by a slowly growing shear layer that transitions approximately one jet diameter downstream into randomly fluctuating, small-scale vortices. This is consistent with previous observations of turbulent round jets (Hussain & Husain 1989).

In contrast to the steady-jet wake, the near-wake of the unsteady propulsor is characterized by more rapid shear layer growth and the roll-up of larger-scale coherent
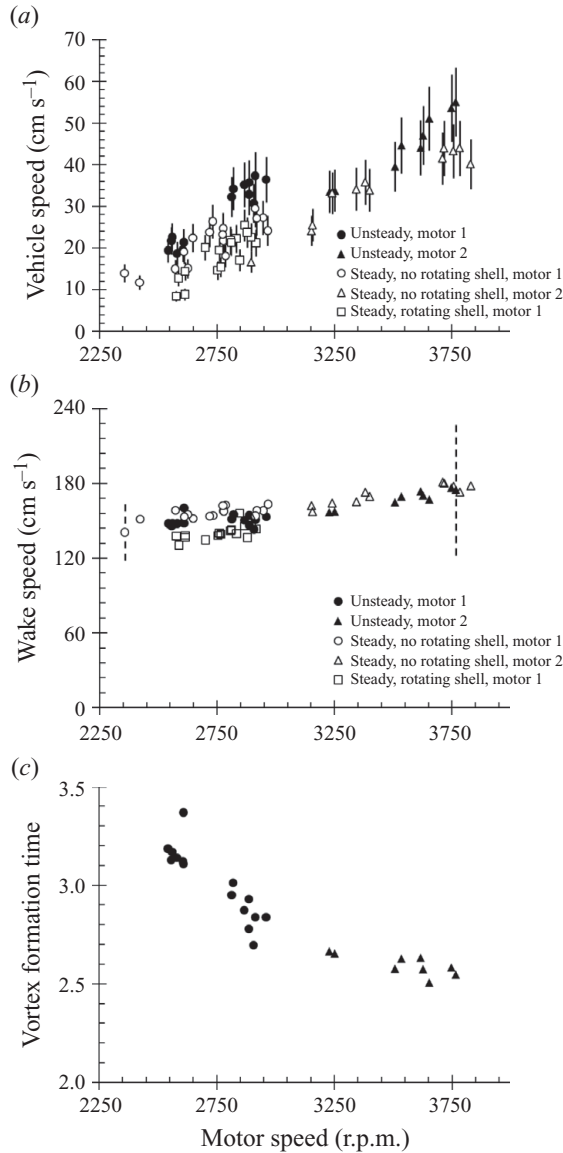
FIGURE 11. (*a*) Vehicle speed versus motor speed. (*b*) Wake speed versus motor speed. (*c*) Vortex formation time versus motor speed. Solid symbols indicate unsteady propulsor and open symbols indicate steady propulsor. Measurement uncertainty in the vehicle velocity was approximately 15 % (indicated by vertical solid lines), and the turbulence fluctuations in the average wake speed varied from 16 % in the low-speed (i.e. motor 1), steady-jet tests to 30 % in the high-speed (i.e. motor 2), unsteady-jet tests (indicated by vertical dashed lines for representative cases).

vortex rings at a fixed temporal frequency. The PLIF images indicate a wider near-wake in the unsteady case, and correspondingly greater ambient fluid entrainment, as evidenced by the significant intrusions of undyed ambient fluid (black) into the dyed nozzle efflux (white).

These qualitative observations were confirmed by DPIV measurements of the stationary vehicle. Figure 13 shows representative images of the vehicle near-wake in
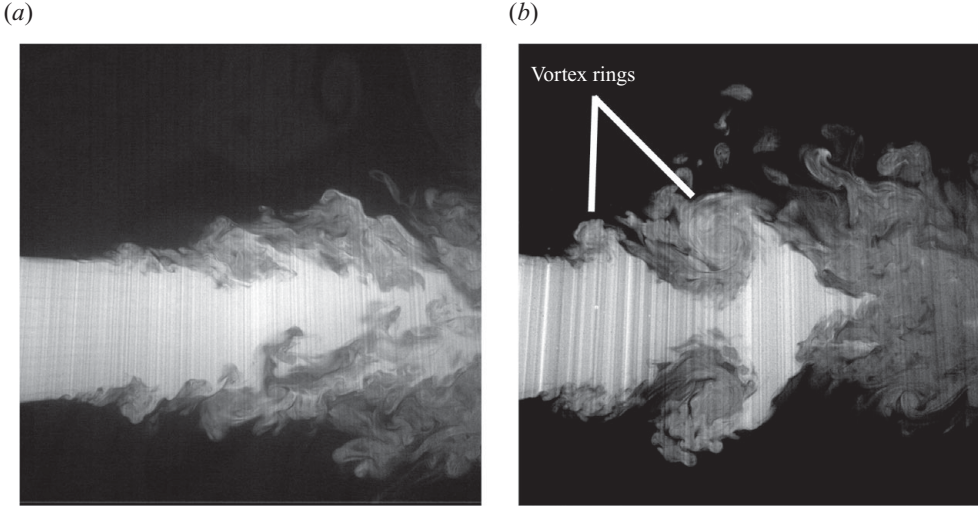
(*a*)   (*b*)

FIGURE 12. PLIF images of the near-wake of the vehicle during steady (*a*) and unsteady (*b*) propulsion. Reynolds number based on jet diameter is approximately 6000 in each case. Pulsing frequency of unsteady jet is approximately 2.4 Hz. Jet diameter is 5.1 cm and nozzle exit plane is at the left edge of the field of view.

steady (figure 13*a*, *c*) and unsteady (figure 13*b*, *d*) propulsion. In agreement with the PLIF visualizations, the steady configuration creates a conventional turbulent jet with relatively uniform speeds in the core flow. In contrast, the unsteady configuration generates discrete vortex rings in the near-wake.

Elevated levels of ambient fluid entrainment are apparent in the increased radial component of velocity vectors in the near-wake of the unsteady propulsor relative to the steady jet. In addition, the magnitude of the near-wake vorticity is increased by over 50 % in the unsteady configuration relative to the steady propulsor. These and other differences in near-wake kinematics are explored in greater detail in the following sections, which focus on the self-propelled vehicle.

5.2. Self-propelled vehicle near-wake

5.2.1. Ambient fluid entrainment

Figure 14 plots the streamwise velocity profile outside the core flow at 0.25 diameters downstream from the nozzle exit plane of the forward-moving, self-propelled vehicle. Data are shown for two motor speeds of the steady propulsor without the rotating cylindrical shell (2900 and 3160 r.p.m., corresponding to $U_w = 1.54$ and $1.57 \, \text{m s}^{-1}$, respectively) and for three motor speeds of the unsteady propulsor (2750, 2970 and 3200 r.p.m., corresponding to $U_w = 1.42$, 1.49 and $1.58 \, \text{m s}^{-1}$, respectively). The steady propulsor was unable to generate sufficient thrust for self-propulsion at motor speeds comparable to the lowest-speed unsteady propulsor test.

Ambient fluid entrainment manifests itself by contributing to a wider wake profile, i.e. larger streamwise velocities outside the core flow. Therefore, the velocity profiles in figure 14 indicate elevated ambient fluid entrainment in the unsteady propulsor near-wake relative to the steady propulsor.

Comparison of the wake velocity profile of the self-propelled, steady propulsor with the wake of the same vehicle in a stationary configuration (cf. figure 13) indicates that the effect of ambient co-flow (in the vehicle reference frame) is minimal. In contrast,
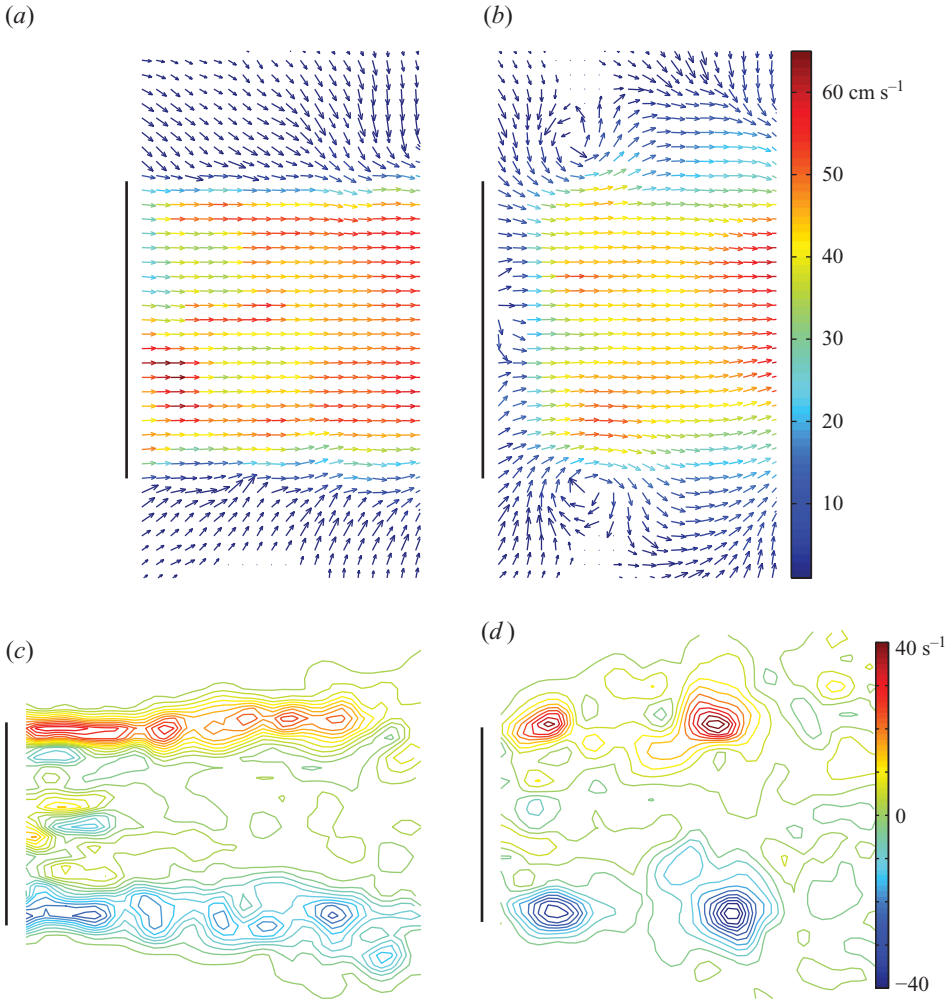
(*a*) (*b*)

(*c*) (*d*)

FIGURE 13. DPIV velocity (*a*, *b*) and vorticity (*c*, *d*) fields from measurements of the near-wake of the vehicle during steady (*a*, *c*) and unsteady (*b*, *d*) propulsion. Reynolds number based on jet diameter is approximately 6000 in each case. Pulsing frequency of unsteady jet is approximately 2.4 Hz. The position and radial extent of the nozzle exit is indicated by the vertical black line in each panel. Colour bars on the right correspond to both panels. Field of view is one jet diameter downstream for velocity fields and two jet diameters downstream for vorticity fields.

entrainment in the near-wake of the unsteady propulsor is reduced by the ambient co-flow around the self-propelled vehicle. This observation is consistent with expectations of reduced wake vortex size and strength due to the reduction of shear-layer strength by the ambient co-flow (Krueger *et al.* 2006).

The velocity measurement near $r/R_{out} = 1$ for the unsteady, medium-speed case in figure 14 is an outlier. Although the origin of the error was not identified conclusively, it appears to be due to a discrepancy between the expected and actual position of the LDV probe in the radial direction during the measurement. The data point is consistent with a lower value of r/R_{out}. As described below, it does not obscure the conclusions derived from the spatially integrated entrainment measurements.
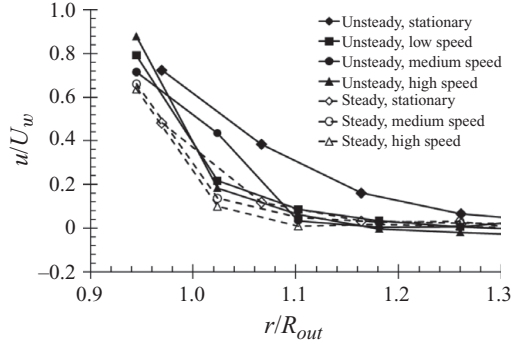
FIGURE 14. Streamwise velocity profiles outside the jet core flow. Solid symbols connected by solid lines indicate unsteady propulsor profiles. Open symbols connected by dashed lines indicate steady propulsor profiles. Data are shown for two motor speeds of the steady propulsor (2900 and 3160 r.p.m., with $U_w = 1.54$ and 1.57 m s^{-1}, respectively) and for three motor speeds of the unsteady propulsor (2750, 2970 and 3200 r.p.m., with $U_w = 1.42$, 1.49 and 1.58 m s^{-1}, respectively). Data from 5 s averages of DPIV measurements at the same downstream location (cf. figure 13) of the stationary steady and unsteady propulsor are also included for comparison.
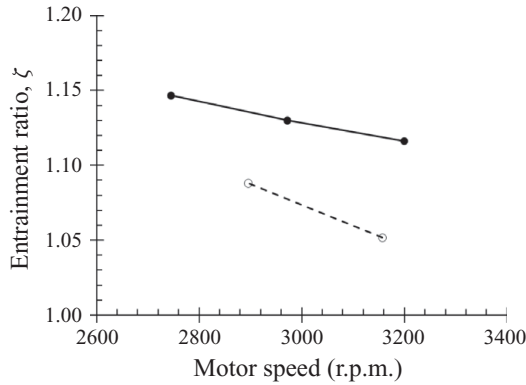

FIGURE 15. Entrainment ratio versus motor speed for the steady propulsor without rotating cylindrical shell (open symbols connected by the dashed line) and the unsteady propulsor (solid symbols connected by the solid line).

The trends in figure 14 are clarified by computing the entrainment ratio ζ (cf. equation (4.1)) for each case. Figure 15 shows that the entrainment ratio decreases with increasing motor speeds. In the unsteady jet, the vortex formation time is inversely proportional to motor speed (figure 11c). Therefore, it appears that entrainment decreases with decreasing vortex formation time. This conclusion is distinct from previous measurements of entrainment by isolated vortex rings, wherein larger vortex rings (i.e. those created with larger formation time) saturate during entrainment and subsequently exhibit slower growth (Dabiri & Gharib 2004; Olcay & Krueger 2008).

Before pursuing this apparent discrepancy further, two important caveats should be noted. First, the present measurements capture the initial advective entrainment that occurs during vortex roll-up. As delineated by Maxworthy (1972), this process of advective entrainment is more rapid than the subsequent diffusive entrainment by fully

formed, steady vortex rings. It is plausible that there is also a different dependence of advective entrainment on vortex formation time than that of the subsequent diffusive entrainment. Second, the present measurements were taken at a single downstream position, whereas the formation length scale of the vortices – and, hence, the downstream position where entrainment occurs – can vary with vortex formation time (Williamson 1996; Bohl & Koochesfahani 2009). A definitive assessment of the dependence of entrainment on vortex formation time would therefore require velocity profile measurements both in the near-wake and at positions further downstream from the nozzle exit. Although such measurements were beyond the scope of the present experiments, they will be needed to reconcile the present near-wake results with previous studies of isolated vortex rings.

In each case, the near-wake entrainment of the pulsed-jet exceeds that of the steady-jet. At the downstream location studied, the difference in entrainment ratio approaches 10 % at higher motor speeds. This difference is significant given that measurement occurred just 0.25 diameters from the nozzle exit plane. The absolute difference in entrainment will increase further with downstream distance as the shear layers grow larger (Hussain & Husain 1989).

The effect that the near-wake entrainment – and vortex formation more generally – has on vehicle performance is described in the following section.

5.2.2. *Vehicle performance*

Figure 16(a) plots the measured Froude efficiency versus motor speed for the various steady and unsteady self-propelled vehicle configurations. The data are normalized by the corresponding Froude efficiency of the steady vehicle in the absence of the cylindrical rotating shell (denoted by η_f^{SWOS}); values greater than one indicate enhanced propulsion, whereas values less than one correspond to reduced performance. The discrete motor speeds at which η_f^{SWOS} was measured were linearly interpolated in a least-squares fit to compute the normalized quantities at other motor speeds in the plot.

At low motor speeds, steady-jet propulsion created by the rotating cylindrical shell is inferior to steady propulsion in the absence of the rotating shell. This result likely reflects the reduced quality of the inflow to the propeller created by the low-solidity rotating shell. Since there was no compensatory benefit in terms of near-wake vortex formation, the overall performance was reduced. The performance of the steady jet with rotating shell does improve with increasing motor speed, but it does not exceed the baseline performance of the steady jet without rotating shell. This result is expected given that the steady-jet propulsion systems are functionally equivalent.

In contrast, the unsteady propulsor consistently outperforms the baseline steady propulsor in terms of Froude efficiency. Increases in efficiency exceeding 40 % are achieved, with modest decreases in the propulsion enhancement at higher motor speeds. The performance at higher motor speeds is consistent with the previous observations that vortex formation time and near-wake entrainment decrease with increasing motor speed (figures 11c and 15).

The trends in Froude efficiency are supported by similar results based on the hydrodynamic efficiency definition in (4.2), plotted in figure 16(b). In this case, the magnitude of vortex enhancement of propulsion is even greater, exceeding 70 % improvement over baseline steady propulsion. Again, modest decreases in vortex enhancement are observed at higher motor speeds, reflecting the formation of smaller vortex rings in that regime.
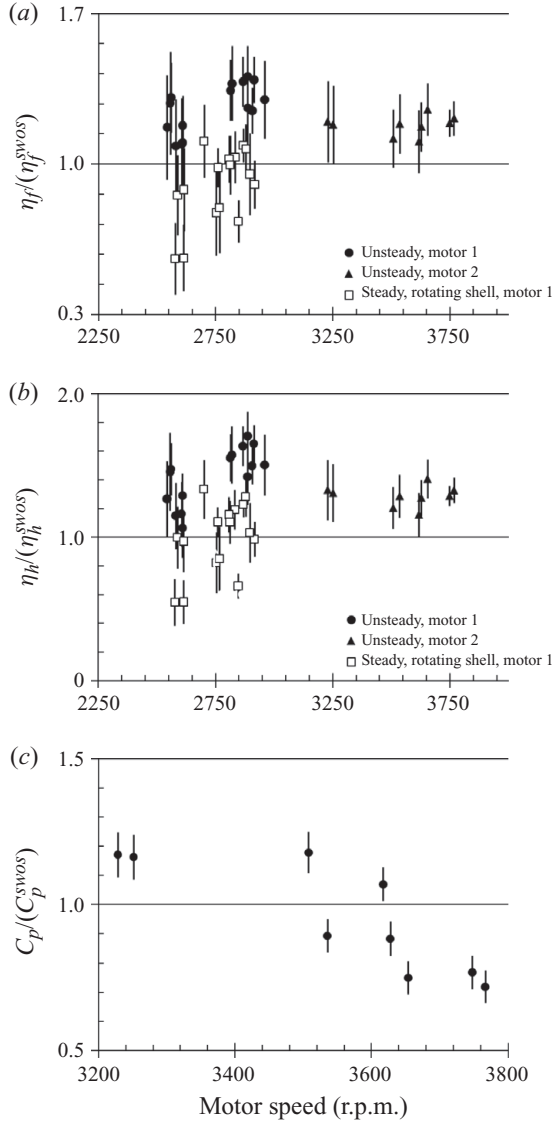
FIGURE 16. (*a*) Normalized Froude efficiency versus motor speed. (*b*) Normalized drag-based hydrodynamic efficiency versus motor speed. (*c*) Normalized power consumption coefficient versus motor speed. Solid symbols indicate unsteady propulsor and open symbols indicate steady propulsor. Normalizations are based on vehicle tests of steady propulsion without a cylindrical rotating shell, denoted by the superscript SWOS.

To determine whether the enhancement of propulsion by near-wake vortex formation compensates for the added energy required to create flow unsteadiness, figure 16(*c*) plots the normalized power consumption coefficient. Values less than one indicate net energy savings by the unsteady propulsor relative to the baseline steady propulsor. The results indicate that at sufficiently high motor speeds, near-wake vortex formation reduces the net energy required for propulsion by as much as 30 % compared to the baseline steady propulsor in these tests. Since vortex ring entrainment becomes less significant at higher motor speeds, we can

attribute the improved performance at higher motor speeds to the more rapid downstream acceleration of the near-wake vortices, i.e. the added-mass effect and associated near-wake pressure elevation described in §2. In addition, the vehicle itself exhibits relatively lower resistance to forward motion at higher speeds (figure 10).

6. Discussion

This paper has demonstrated an experimental platform to directly compare steady and unsteady propulsion of a self-propelled vehicle. An analytical model of the near-wake created by the unsteady vehicle predicted that vortex formation in the near-wake – specifically, ambient fluid entrainment and added-mass dynamics of the accelerated flow – could potentially enhance propulsion relative to a conventional, steady-jet system. Measurements of the near-wake confirmed the existence of large-scale vortex roll-up by the unsteady propulsor and elevated entrainment of ambient fluid. These processes led to improvements in Froude efficiency of up to 40 % and increases in a drag-based hydrodynamic efficiency metric of over 70 % relative to the baseline steady propulsor configuration.

A unique result of this study is the demonstration of a net reduction in power consumption of the unsteady propulsor, accounting for the power required to create flow unsteadiness. This result is important for establishing the viability of vortex-enhanced propulsion in practice. Previous attempts to improve propulsion by unsteady manipulation of the mean flow (e.g. biomimetic propulsion) have often neglected to assess the net power requirements relative to conventional steady propulsion.

It is important to draw a distinction between the results of this study that are specific to the vehicle platform studied presently and those results that are general to vortex-enhanced propulsion. As mentioned in §3, the vehicle design implemented here has not been optimized for hydrodynamic efficiency in an absolute sense. The flow-chopping mechanism introduces hydrodynamic losses within the inlet housing, and the propeller used in the experiments was not tuned to the unsteady inflow conditions. These losses are evident from the fact that the steady propulsor with rotating shell in the inlet housing performed poorly relative to the steady propulsor in the absence of the rotating shell (figure 16*a*, *b*), despite the fact that the rotating shell possessed negligible solidity. The enhancement in performance of the unsteady propulsor was sufficient to compensate for inefficiencies of the inlet flow while still improving propulsion relative to the baseline steady propulsor without the rotating shell. Nonetheless, the absolute values of the Froude and drag-based hydrodynamic efficiency did not exceed 50 and 65 %, respectively, in the unsteady propulsor.

Despite these shortcomings of the vehicle design, the results make clear the potential benefits of vortex-enhanced propulsion. The existence of the two primary mechanisms of enhanced propulsion – namely (i) ambient fluid entrainment by the forming vortex ring and (ii) downstream acceleration of the vortex ring, its entrained fluid mass and their added-mass – is not dependent on the specific vehicle design studied here. Future work will seek to identify more efficient mechanisms to promote the formation and acceleration of coherent vortices in the near-wake of the propulsor. Several candidates are found in the existing literature, including modifications of nozzle ellipticity (Hussain & Husain 1989) and periodic excitation of the boundary layers at the nozzle exit (Reynolds *et al.* 2003). These strategies can potentially be achieved by

active or passive (i.e. zero net energy input) mechanisms. Passive mechanisms present the greatest potential for net power reduction in engineered propulsion systems, and can also facilitate retrofitting of existing propulsion systems to take advantage of the processes described in this paper.

The parameter space of vortex formation time presents an additional opportunity to further amplify vortex-enhanced propulsion. In the present experiments, the vortex formation time and, hence, the size of the wake vortices, was dictated by the slot geometry and motor speed. The generated vortex rings did not approach the maximum vortex size observed in previous studies of stationary propulsors, for which $\hat{T} \approx 4$ (Gharib *et al.* 1998). It is of interest to determine how vortex-enhanced propulsion is affected for $\hat{T} > 4$. Previous studies suggest that an optimum vortex formation time may exist for propulsion (Linden & Turner 2004; Krueger & Gharib 2005; Krieg & Mohseni 2008; Dabiri 2009).

An aspect of propulsion that has only been addressed indirectly here is that of the pressure in the near-wake. The derivation in §2 indicates that a principal origin of vortex-enhanced propulsion is the elevated near-wake pressure. We have shown that this pressure can be understood in terms of vortex added-mass; however, it would be illuminating to examine the pressure field directly. Pressure measurements would also be useful to test the various assumptions used to construct the analytical model in §2. Such an endeavour was beyond the scope of this study, but in practice could be accomplished by implementing surface pressure probes in the nozzle if the probes and auxiliary equipment could be made to move with the vehicle. A more straightforward approach may be to simulate these processes numerically. In that case, the primary challenges will be simulating self-propulsion and approaching the Reynolds numbers of the experiments ($Re \approx 10^5$).

Much of the inspiration for new unsteady propulsion approaches has come from biology in recent years. The analytical model developed in §2 can potentially be extended to support studies of biological propulsion, where the formation of near-wake vortices is ubiquitous. Although it is unclear whether propulsion in the absence of vorticity might be preferable (it is feasible, cf. Kanso *et al.* 2005), we suggest that biology may exploit the unsteady mechanisms described in this paper to take advantage of the vortices that are inevitably created during locomotion in real fluids.

REFERENCES

BATCHELOR, G. K. 2000 *An Introduction to Fluid Dynamics*. Cambridge University Press.

BINDER, G. & DIDELLE, H. 1981 Improvement of ejector thrust augmentation by pulsating or flapping jets. Proc. AGARD Conf. Fluid Dynamics of Jets with Applications to V/STOL, Lisbon, Portugal, vol. 308, pp. 1–11.

BLAUROCK, J. 1990 An appraisal of unconventional aftbody configurations and propulsion devices. *Mar. Tech.* **27**, 325–336.

BOHL, D. G. & KOOCHESFAHANI, M. F. 2009 MTV measurements of the vortical field in the wake of an airfoil oscillating at high reduced frequency. *J. Fluid Mech.* **620**, 63–88.

BRESLIN, J. P. & ANDERSEN, P. 1996 *Hydrodynamics of Ship Propellers*. Cambridge University Press.

CHOUTAPALLI, I. M., ALKISLAR, M. B., KROTHAPALLI, A. & LOURENCO, L. M. 2005 An experimental study of pulsed jet ejector. *AIAA paper* 2005-1208.

Cox, B. D. & Reed, A. M. 1988 Contrarotating propellers: design theory and applications. In *Proceedings of the Propellers '88 Symposium*, pp. 15.1–15.29.

Dabiri, J. O. 2006 Note on the induced Lagrangian drift and added-mass of a vortex. *J. Fluid Mech.* **547**, 105–113.

Dabiri, J. O. 2009 Optimal vortex formation as a unifying principle in biological propulsion. *Annu. Rev. Fluid Mech.* **41**, 17–33.

Dabiri, J. O. & Gharib, M. 2004 Fluid entrainment by isolated vortex rings. *J. Fluid Mech.* **511**, 311–331.

Gharib, M., Rambod, E. & Shariff, K. 1998 A universal time scale for vortex ring formation. *J. Fluid Mech.* **360**, 121–140.

Glover, E. J. 1987 Propulsive devices for improved propulsive efficiency. *Trans. Inst. Mar. Engrs* **99**, 23–29.

Grim, O. 1980 Propeller and vane wheel. *J. Ship Res.* **24**, 203–226.

Grothues-Spork, H. 1988 Bilge vortex control devices and their benefits for propulsion. *Intl Shipbuilding Prog.* **35**, 183–214.

Hadler, J. B. 1969 Contrarotating propeller propulsion: a state-of-the-art report. *Mar. Tech.* **6**, 281–289.

Hill, M. J. M. 1894 On a spherical vortex. *Phil. Trans. R. Soc. Lond.* A **185**, 213–245.

Hoerner, S. F. 1965 *Fluid-Dynamic Drag*. Hoerner Fluid Dynamics.

Houghton, E. L. & Carpenter, P. W. 2003 *Aerodynamics*. Elsevier.

Hussain, F. & Husain, H. S. 1989 Elliptic jets. Part 1. Characteristics of unexcited and excited jets. *J. Fluid Mech.* **208**, 257–320.

Kanso, E., Marsden, J. E., Rowley, C. W. & Melli-Huber, J. B. 2005 Locomotion of articulated bodies in a perfect fluid. *J. Nonlinear Sci.* **15**, 255–289.

Krieg, M. & Mohseni, K. 2008 Thrust characterization of a bioinspired vortex ring thruster for locomotion of underwater robots. *IEEE J. Ocean. Engng* **33**, 123–132.

Krueger, P. S. 2001 The significance of vortex ring formation and nozzle exit over-pressure to pulsatile jet propulsion. PhD thesis, California Institute of Technology.

Krueger, P. S., Dabiri, J. O. & Gharib, M. 2006 The formation number of vortex rings formed in uniform background co-flow. *J. Fluid Mech.* **556**, 147–166.

Krueger, P. S. & Gharib, M. 2003 The significance of vortex ring formation to the impulse and thrust of a starting jet. *Phys. Fluids* **15**, 1271–1281.

Krueger, P. S. & Gharib, M. 2005 Thrust augmentation and vortex ring evolution in a fully pulsed jet. *AIAA J.* **43**, 792–801.

Linden, P. F. & Turner, J. S. 2004 'Optimal' vortex rings and aquatic propulsion mechanisms. *Proc. R. Soc. Lond.* B **271**, 647–653.

Lockwood, R. M. 1961 Interim summary report on investigation of the process of energy transfer from an intermittent jet to secondary fluid in an ejector-type thrust augmenter. *Hiller Aircraft Rep.* ARD-286.

Maxworthy T. 1972 The structure and stability of vortex rings. *J. Fluid Mech.* **51**, 15–32.

Moslemi, A. A. & Krueger, P. S. 2010 Propulsive efficiency of a bio-inspired pulsed-jet underwater vehicle. *Bioinspir. Biomim.* **5**, 036003.

Narita, H., Yagi, H., Johnson, H. D. & Breves, L. R. 1981 Development and full-scale experiences of a novel integrated duct propeller. *Trans. SNAME* **89**, 319–346.

Norbury, J. 1973 A family of steady vortex rings. *J. Fluid Mech.* **57**, 417–431.

Olcay, A. B. & Krueger, P. S. 2008 Measurement of ambient fluid entrainment during laminar vortex ring formation. *Exp. Fluids* **44**, 235–247.

Paxson, D. E., Litke, P. J., Schauer, F. R., Bradley, R. P. & Hoke, J. L. 2006 Performance assessment of a large scale pulsejet-driven ejector system. *NASA Tech. Memo.* 2006-214224.

Prandtl, L. 1952 *Essentials of Fluid Dynamics*. Hafner.

Prandtl, L. & Tietjens, O. G. 1934 *Applied Hydro- and Aeromechanics*. Dover.

Reynolds, W. C., Parekh, D. E., Juvet, P. J. D. & Lee, M. J. D. 2003 Bifurcating and blooming jets. *Annu. Rev. Fluid Mech.* **35**, 295–315.

Sachs, A. H. & Burnell, J. A. 1962 Ducted propellers: a critical review of the state of the art. *Prog. Aeronaut. Sci.* **3**, 85–135.

SAFFMAN, P. G. 1992 *Vortex Dynamics*. Cambridge University Press.

SCHLICHTING, H. & GERSTEN, K. 2000 *Boundary-Layer Theory*. Springer.

SHADDEN, S. C., DABIRI, J. O. & MARSDEN, J. E. 2006 Lagrangian analysis of fluid transport in empirical vortex ring flows. *Phys. Fluids* **18**, 047105.

STIPA, L. 1931 Experiments with intubed propellers. *NACA Tech. Rep.* TM 655.

WILLIAMSON, C. H. K. 1996 Vortex dynamics in the cylinder wake. *Annu. Rev. Fluid Mech.* **28**, 477–539.

WU, T. Y. 1962 Flow through a heavily loaded actuator disc. *Schiffstechnik* **9**, 134–138.